Mon. Not. R. Astron. Soc. **000**, 1–14 (2014) Printed 24 January 2014 (MN LATEX style file v2.2)

The dynamics of isolated Local Group galaxies⋆

Evan N. Kirby,[1]†‡ James S. Bullock,[1] Michael Boylan-Kolchin,[2]
Manoj Kaplinghat[1] and Judith G. Cohen[3]
[1]*Department of Physics and Astronomy, University of California, 4129 Frederick Reines Hall, Irvine, California 92697, USA*
[2]*Department of Astronomy and Joint Space-Science Institute, University of Maryland, College Park, Maryland 20742, USA*
[3]*Department of Astronomy & Astrophysics, California Institute of Technology, 1200 E. California Blvd., MC 249-17, Pasadena, CA 91125, USA*

Accepted 2014 January 6. Received 2013 December 20; in original form 2013 October 31

ABSTRACT
We measured velocities of 862 individual red giant stars in seven isolated dwarf galaxies in the Local Group: NGC 6822, IC 1613, VV 124 (UGC 4879), the Pegasus dwarf irregular galaxy (DDO 216), Leo A, Cetus, and Aquarius (DDO 210). We also computed velocity dispersions, taking into account the measurement uncertainties on individual stars. None of the isolated galaxies is denser than the densest Local Group satellite galaxy. Furthermore, the isolated dwarf galaxies have no obvious distinction in the velocity dispersion–half-light radius plane from the satellite galaxies of the Milky Way and M31. The similarity of the isolated and satellite galaxies' dynamics and structural parameters imposes limitations on environmental solutions to the too-big-to-fail problem, wherein there are fewer dense dwarf satellite galaxies than would be expected from cold dark matter simulations. This data set also has many other applications for dwarf galaxy evolution, including the transformation of dwarf irregular into dwarf spheroidal galaxies. We intend to explore these issues in future work.

Key words: Local Group – galaxies: dwarf – galaxies: kinematics and dynamics.

1 INTRODUCTION

Nearby dwarf galaxies are excellent laboratories to study galactic dynamics, chemical evolution and dark matter physics. They lend themselves so well to detailed scrutiny because they are close enough for resolved stellar spectroscopy. Multi-object spectrographs on 8–10 m telescopes, like Keck/DEIMOS (Faber et al. 2003), Gemini/GMOS (Hook et al. 2004), VLT/FORS2 (Appenzeller et al. 1998) and VLT/FLAMES (Pasquini et al. 2002), can amass sample sizes of hundreds of stellar spectra for galaxies as far away as $\sim$ 1.5 Mpc. Even with low signal-to-noise (S/N) ratios, it is possible to measure radial velocities with typical precisions of 2–5 km s^{-1}. Higher quality spectra permit measurements of metallicities (e.g., Tolstoy et al. 2001) and even detailed abundance ratios (e.g., Kirby et al. 2009; Letarte et al. 2010).

The Milky Way's satellite galaxies are the best-studied dwarfs in the Local Volume because of their proximity. Recent large surveys like the Spectroscopic and Panchromatic Landscape of Andromeda's Stellar Halo (SPLASH, Guhathakurta et al. 2005, 2006), the Pan-Andromeda Archaeological Survey (PAndAS, McConnachie et al. 2009) and the Panchromatic Hubble Andromeda Treasury (PHAT, Dalcanton et al. 2012) have increased the accessibility of M31 and its satellites. The isolated dwarf galaxies in the field of the Local Group are more difficult to discover and to observe because they are more distant than the Milky Way satellites, and they span the entire sky, unlike the M31 satellites.

The structural properties of dwarf galaxies may be influenced by their environments. For example, a large host galaxy may induce tidal stripping and deformation (e.g., Peñarrubia, Navarro & McConnachie 2008). Proximity to a large galaxy also strongly correlates with a dwarf galaxy's gas content (e.g., Knapp, Kerr, & Bowers 1978; Grcevich & Putman 2009), star formation history (e.g., Grebel et al. 2003; Weisz et al. 2011) and morphology (e.g., Binggeli, Tarenghi, & Sandage 1990; Lisker et al. 2007). The isolation of Local Group galaxies that are far from the Milky Way or M31 insulates them from tides and ram pressure. It is possible that some of the isolated Local

⋆ The data presented herein were obtained at the W. M. Keck Observatory, which is operated as a scientific partnership among the California Institute of Technology, the University of California and the National Aeronautics and Space Administration. The Observatory was made possible by the generous financial support of the W. M. Keck Foundation.
† Center for Galaxy Evolution Fellow.
‡ E-mail: ekirby@uci.edu

Group dwarf galaxies passed near a large galaxy but did not become bound ('backsplash galaxies,' Sales et al. 2007; Teyssier, Johnston & Kuhlen 2012). An otherwise isolated dwarf galaxy can also interact with another dwarf galaxy or even a dark subhalo (Helmi et al. 2012). Despite these possible disturbances, the field of the Local Group is the best place to study the evolution of dwarf galaxies that have survived unmolested for the age of the Universe.

There are compelling reasons for comparing the dynamical properties of satellite galaxies to isolated galaxies. Such comparisons are likely to shed light on formation and evolution mechanisms for both dwarf irregular (dIrr) and dwarf spheroidal (dSph) galaxies. It is now known that these two classes of galaxies share the same stellar mass–stellar metallicity relation (Kirby et al. 2013b), which limits the amount of stellar stripping associated with possible transformations of dIrrs to dSphs. Dynamical measurements should provide further and complementary constraints.

Furthermore, comparing the dynamics of isolated galaxies to satellite galaxies can inform possible solutions to the 'too big to fail' problem (TBTF, Boylan-Kolchin, Bullock & Kaplinghat 2011, 2012). Cold dark matter simulations predict more dense dark matter subhaloes than are observed among the Milky Way satellite galaxies. The problem also exists for the M31 system (Tollerud et al. 2012, 2013; Collins et al. 2013). One way to alleviate TBTF is to invoke baryonic physics, wherein energy injection from gas and stars alters the mass profiles of the dark matter subhaloes (e.g., Brooks et al. 2013). High-resolution hydrodynamical simulations (e.g., Zolotov et al. 2012), analytic arguments (Peñarrubia et al. 2012) and idealized numerical simulations (Garrison-Kimmel et al. 2013) indicate energy injection alone is unlikely to fully explain TBTF because the low stellar content of the Milky Way satellites places a strong limit on the amount of feedback available (though see Amorisco, Zavala & de Boer 2013). Environmental effects such as tides and ram pressure are therefore central to baryonic solutions to TBTF (Arraki et al. 2013; Brooks & Zolotov 2012). For that reason, it is important to measure the kinematic and structural properties for isolated dwarf galaxies in the field of the Local Group and compare them to dwarf satellites.

Stellar velocity measurements are already available for seven isolated dwarf galaxies. Tolstoy et al. (2001) measured the velocities for 23 red giants in the dIrr NGC 6822, but the primary purpose of their survey was to measure the metallicity distribution. Demers, Battinelli & Kunkel (2006) also measured the velocities of 110 carbon stars in NGC 6822, but the intrinsic variability of the stars limited the velocity precision to ~ 15 km s^{-1}, larger than the velocity dispersion of any Milky Way dSph. Leaman et al. (2009, 2012) measured the velocities of 180 red giants in the WLM dIrr. They found a stellar rotation velocity about equal to the velocity dispersion. They also calculated a very large mass within the half-light radius ($(4.3 \pm 0.3) \times 10^8$ M$_\odot$), which is perhaps appropriate for its large half-light radius (1.6 kpc). Kirby, Cohen & Bellazzini (2012) observed 67 red giants in VV 124 (UGC 4879). They found that most of the mass within the half-light radius of VV 124 is dark matter despite the relatively small half-light radius (272 pc). Brown et al. (2007) observed ten B supergiants in Leo A. From these young stars, they determined that Leo A's dynamical mass is at least five times its stellar mass. Lewis et al. (2007) also measured a very high dynamical mass-to-light ratio for the Cetus dSph. However, the quality of their spectra yielded a mean velocity uncertainty of 8.8 km s^{-1}. Fraternali et al. (2009) measured both dispersion and rotation in Tucana. Both values are similar to those for WLM, which is surprising given Tucana's low luminosity (6×10^5 L$_\odot$). Finally, Simon & Geha (2007) measured the velocity dispersion for Leo T and seven other ultra-faint dwarf galaxies. Leo T is probably the only recently discovered (Irwin et al. 2007) ultra-faint galaxy near the Milky Way that is on its first infall. Regardless, its mass-to-light ratio is very high (~ 90 M$_\odot$ L$_\odot^{-1}$), like the other ultra-faint galaxies.

In this contribution, we expand the kinematic observations of isolated dwarf galaxies. We refine the kinematic measurements for NGC 6822, Leo A and Cetus. We also provide velocity dispersions for isolated dwarf galaxies without previous measurements: IC 1613, the Pegasus dIrr (DDO 216) and Aquarius (DDO 210). We also include our previous kinematic measurements of VV 124 (Kirby et al. 2012). In Secs. 2 and 3, we describe our spectroscopy and measurements of individual stellar velocities. We provide a table of velocities so that others may construct their own dynamical models of these galaxies. We rule stars as members and non-members of their respective galaxies in Sec. 4. In Sec. 5, we describe the calculation of velocity dispersions. Finally, we compare the kinematic and structural properties of isolated dwarf galaxies to dwarf satellites of the Milky Way and M31 in Sec. 6.

2 OBSERVATIONS

We observed seven isolated galaxies in the Local Group with the Deep Imaging Multi-object Spectrograph (DEIMOS, Faber et al. 2003) on the Keck II telescope. Table 1 summarises our observations. Kirby et al. (2012, 2013b) already presented the observations of most these galaxies. We add observations of Cetus to these published data.

We selected Cetus targets in the same manner as the other dwarf galaxies (Kirby et al. 2012, 2013b). A. McConnachie and M. Irwin kindly provided us their photometric catalogue from the Wide Field Camera on the Isaac Newton Telescope (McConnachie & Irwin 2006). We designed two DEIMOS slitmasks centred on Cetus. Fig. 1 shows the positions and orientations of the slitmasks in celestial coordinates. It also identifies stars that we later determined to be spectroscopic members and non-members (Sec. 4).

Targets were selected to have the colours and magnitudes of red giants, assuming a distance modulus of $(m - M)_0 = 24.46$ (Bernard et al. 2009) and a reddening of $E(B-V) = 0.029$ (Schlegel, Finkbeiner & Davis 1998). In practice, we chose stars with $20.4 < i_0' < 24.0$ and colours within 0.3 mag of a 12.6 Gyr Padova isochrone (Girardi et al. 2002) with [Fe/H] $= -1.6$. We then added other objects outside of this selection region in order to fill the slitmask. Fig. 2 shows the colour–magnitude diagram from the photometric catalogue (McConnachie & Irwin 2006). Spectroscopic targets, including members and non-members (determined as described in Sec. 4) are indicated with large symbols.

We observed the first Cetus slitmask, ceta, on 2013 September 1. We observed the second slitmask, cetb, on

Table 1. Summary of DEIMOS observations.

Galaxy	Slitmask	# Targets	Exposure Time (h)	Originally Published By
IC 1613	i1613a	199	10.3	Kirby et al. (2013b)
NGC 6822	n6822a	180	8.7	Kirby et al. (2013b)
	n6822b	180	6.0	Kirby et al. (2013b)
VV 124	vv124a	121	3.7	Kirby et al. (2012)
	vv124b	120	3.8	Kirby et al. (2012)
Pegasus	pega	113	6.8	Kirby et al. (2013b)
Leo A	leoaaW	91	6.7	Kirby et al. (2013b)
Cetus	ceta	146	5.8	this work
	cetb	131	5.8	this work
Aquarius	aqra	64	8.9	Kirby et al. (2013b)

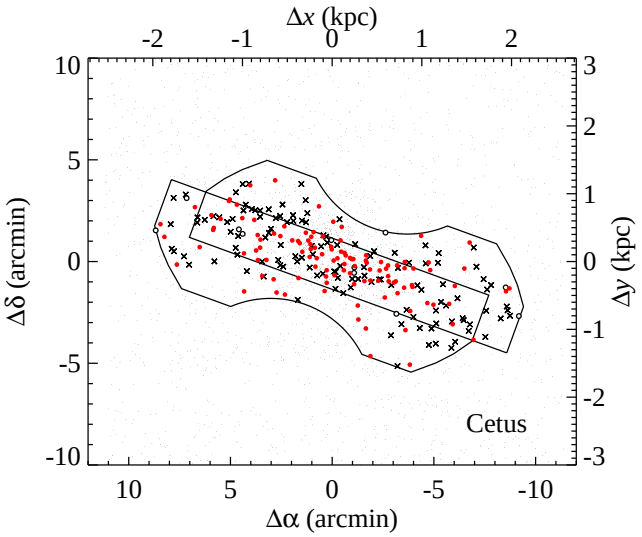

Figure 1. The sky position of the two Keck/DEIMOS slitmasks for Cetus. Filled, red points are spectroscopically confirmed members. Hollow, black points are non-members. Crosses are spectroscopic targets for which it was not possible to measure a velocity. The origin is $\alpha_0 = 00^{\rm h}26^{\rm m}11^{\rm s}$, $\delta_0 = -11°02'40''$. The top and right axes give the projected distance from the centre of Cetus in kpc for an assumed distance of 779 kpc (Bernard et al. 2009).

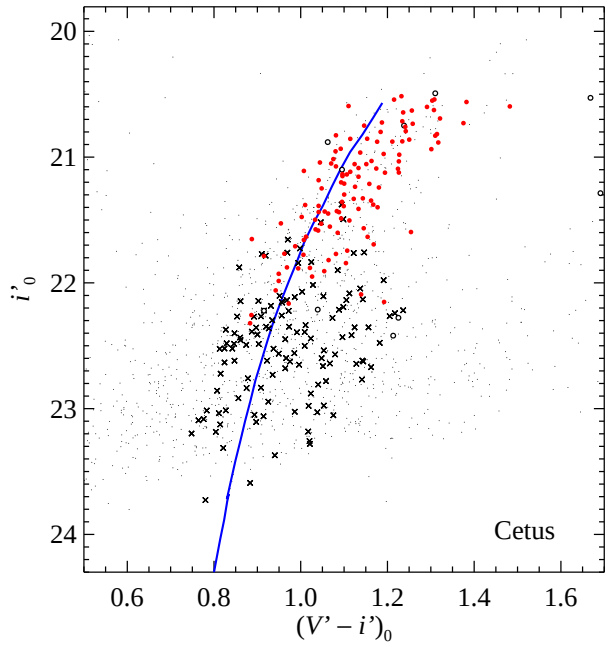

Figure 2. The extinction- and reddening-corrected colour–magnitude diagram for Cetus from the photometry catalogue of McConnachie & Irwin (2006). The filters are Johnson V' and Gunn i'. Symbols have the same meanings as Fig. 1. The blue line is a 12.6 Gyr Padova isochrone (Girardi et al. 2002) with [Fe/H] $= -1.6$ at a distance modulus of $(m - M)_0 = 24.46$ (Bernard et al. 2009).

the next night. We obtained 12 exposures for each slitmask with a total exposure time of 350 minutes (5.8 hours) per slitmask. The sky was clear on both nights. The seeing was about 0.″9 for the first night, but the seeing varied between 1.″0 and 1.″5 for most of the second night before settling to 0.″9 for the last hour.

The spectrograph was configured in the same manner for all of the observations. We used the 1200G grating with a groove spacing of 1200 mm^{-1} and a blaze wavelength of 7760 Å. The grating was tilted so that first-order light spanned about 6400–9000 Å across the CCD mosaic. The central wavelength of each spectrum was approximately 7800 Å, but the exact spectral range depended on the placement of the slit along the slitmask. The slit widths were 0.″7 for all slitmasks except for Leo A, for which the slit widths were 1.″1. The resolving powers for the two slit widths at 8500 Å were $R \sim 7100$ and 4700, respectively. We reduced the data into sky-subtracted, one-dimensional spectra with the SPEC2D software pipeline (Cooper et al. 2012; Newman et al. 2013).

3 VELOCITY MEASUREMENTS

We measured radial velocities by cross-correlating the observed spectra with templates also observed with DEIMOS. J. Simon and M. Geha kindly provided the same templates they used to measure velocities of red giants in ultra-faint dwarf galaxies (Simon & Geha 2007). The templates included red giants at a variety of metallicities as well as a few K and M dwarfs.

Before cross-correlation, we normalized the observed spectrum. We fitted a B-spline with a breakpoint every 100 pixels to 'continuum regions' that Kirby, Guhathakurta & Sneden (2008) determined to be largely free of absorption lines. The continuum regions also excluded telluric absorption. The B-spline fit was weighted by the inverse variance of each pixel. For more details on

the continuum division, please refer to Kirby et al. (2009, sec. 3.4).

Following the same procedure as Simon & Geha (2007), we computed the velocity of the maximum cross-correlation for each of the 16 template spectra. In contrast to Simon & Geha, we used only the red half of the spectrum. The DEIMOS focal plane is an eight-CCD mosaic. The CCDs are distributed in two rows of four detectors. Each stellar spectrum spans two CCDs. The SPEC2D reduction code computes separate velocity solutions for the red and blue chips. In order to eliminate any systematic difference between the two wavelength solutions, we used the half of the spectrum only from the red CCD to compute the velocity. This half of the spectrum includes the Ca II near-infrared triplet at 8498, 8542 and 8662 Å. These absorption lines dominate the cross-correlation.

We adopted the velocity corresponding to the template with the lowest reduced χ^2. We shifted this velocity to the heliocentric frame based on the position in the sky and the time of observation. We checked every spectrum by eye to ensure that the observed spectrum lined up with the best-matching template spectrum. In the rare cases where the velocity was obviously wrong, we excluded certain regions of the spectrum, such as the margins of the CCD where vignetting can cause a sharp dip in flux, and we recomputed the velocity.

We estimated the Monte Carlo error on the velocity by resampling the spectrum 1000 times. In each Monte Carlo realisation, we added a random value to the continuum-normalized flux in each pixel. The random value was chosen from a normal distribution with a standard deviation equal to the estimated continuum-normalized variance on the pixel flux. We recomputed the velocity that maximized the cross-correlation using the best-fitting template spectrum determined above.

Simon & Geha (2007) found that the Monte Carlo error is an incomplete description of the total error on velocity. From repeat measurements of red giants in ultra-faint dwarf galaxies, they determined a systematic error floor of 2.2 km s^{-1}. Kirby et al. (2012, 2013a) repeated this exercise with the isolated dIrr VV 124 and the ultra-faint dSph Segue 2. They determined error floors of 2.21 km s^{-1} and 1.95 km s^{-1}. Our sample contains very few repeat measurements other than the VV 124 sample already analysed by Kirby et al. (2012). Therefore, we adopt a systematic error of 2.1 km s^{-1}, which we added in quadrature to the random uncertainties determined from the Monte Carlo resampling. The velocity dispersions for the isolated dwarf galaxies in this paper are at least several times this systematic error. Hence, the difference between 2.21 km s^{-1} and 1.95 km s^{-1} is inconsequential.

Fig. 3 shows some example spectra at a range of S/N. The S/N was calculated as the median absolute deviation from the continuum in the continuum regions. (See sec. 2.3 of Kirby et al. 2012 for more details.) The figure also shows the best-matching template spectra. The Ca triplet line strengths do not necessarily match between the two spectra, but the spectra align in wavelength.

The S/N is quite low in the lowest quality spectra, such as M05–3901 in Fig. 3. However, cross-correlation can identify patterns in spectral features that are not easy to see by eye. It is nonetheless worthwhile to validate velocity mea-

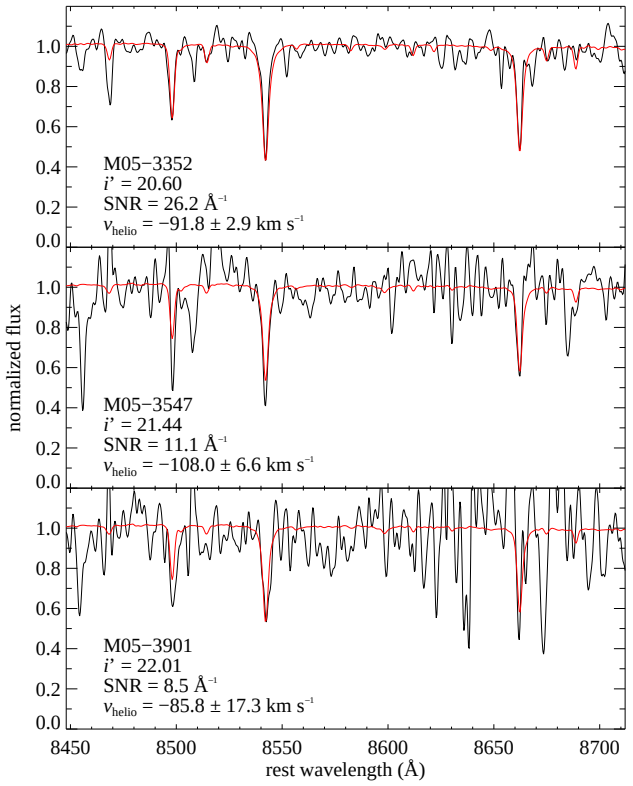

Figure 3. Examples of DEIMOS spectra of red giants in the Cetus dSph. The black lines show the DEIMOS spectra smoothed with a Gaussian with FWHM = 1.6 Å. The red lines show the best-fitting radial velocity template spectra. The top spectrum has among the highest S/N in the Cetus sample, and the bottom has among the lowest S/N.

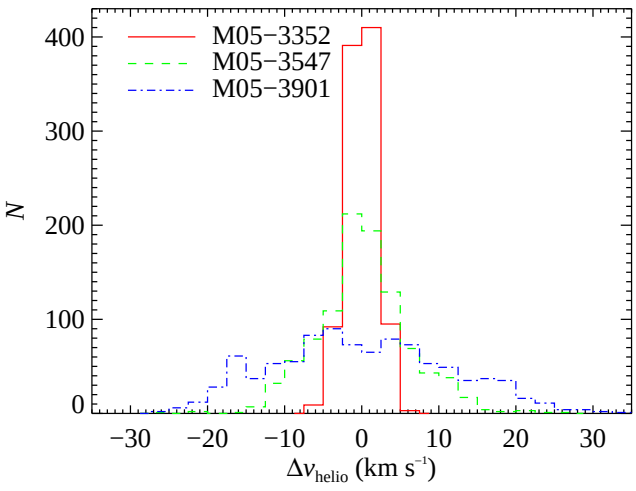

Figure 4. Probability distributions for the radial velocities of the spectra shown in Fig. 3. The histograms show the distribution of the differences between the measured $v_{\rm helio}$ and the velocities for 1000 Monte Carlo trials.

Table 2. Catalogue of velocities for individual stars.

Galaxy	Object Name	RA (J2000)	Dec (J2000)	S/N (Å^{-1})	$v_{\rm helio}$ (km s^{-1})	Member?	Reason
IC 1613	B07-44743	01 04 22.55	+02 09 33.3	28.2	-254.2 ± 2.6	Y	
IC 1613	B07-44686	01 04 23.06	+02 10 09.1	20.4	-237.1 ± 3.0	Y	
IC 1613	B07-41610	01 04 23.30	+02 08 50.8	26.6	-263.9 ± 2.6	N	v
IC 1613	B07-44467	01 04 25.31	+02 10 29.2	12.3	-240.4 ± 5.6	Y	
IC 1613	B07-44459	01 04 25.40	+02 11 02.6	19.6	-231.5 ± 3.2	Y	
IC 1613	B07-37893	01 04 25.53	+02 08 39.0	19.9	-242.3 ± 2.7	Y	
IC 1613	B07-47494	01 04 26.16	+02 11 47.9	13.3	-244.0 ± 4.3	Y	
IC 1613	B07-41149	01 04 26.26	+02 10 22.3	34.3	-252.5 ± 2.3	Y	
IC 1613	B07-47458	01 04 26.98	+02 11 50.5	13.3	-243.8 ± 3.9	Y	
IC 1613	B07-41044	01 04 27.32	+02 10 35.1	20.3	-249.0 ± 3.0	Y	

'Reason' indicates reasons for non-membership. v: Radial velocity non-member. Na: Na I λ8190 EW exceeds 1 Å. This table has 862 rows, of which only the first 10 rows are reproduced here.

surements for cases that seem questionable. Fig. 4 shows the results of the 1000 Monte Carlo trials of measuring $v_{\rm helio}$ for the three spectra shown in Fig. 3. Even in the case of the lowest S/N, the velocities are distributed roughly normally about the measured velocity. If the spectrum contained no useful information, the velocities from the 1000 trials would be distributed uniformly over the velocity range that the cross-correlation searched. Furthermore, there is only one peak in each probability distribution. Therefore, the cross-correlation found a unique velocity for each star.

It was not possible to measure velocities of some stars because the S/N was too low. If we could identify no clear Ca triplet in the spectrum, then we marked the spectrum as unusable. We also excluded from our sample all stars with velocity errors in excess of 30 km s^{-1}. Stars with unusable spectra are marked as crosses in Figs. 1 and 2.

Table 2 gives the celestial coordinates, S/N ratios, heliocentric radial velocities and velocity uncertainties (random and systematic errors added in quadrature) for each star in all seven dwarf galaxies. It also includes information about our membership determinations for each star (see Sec. 4).

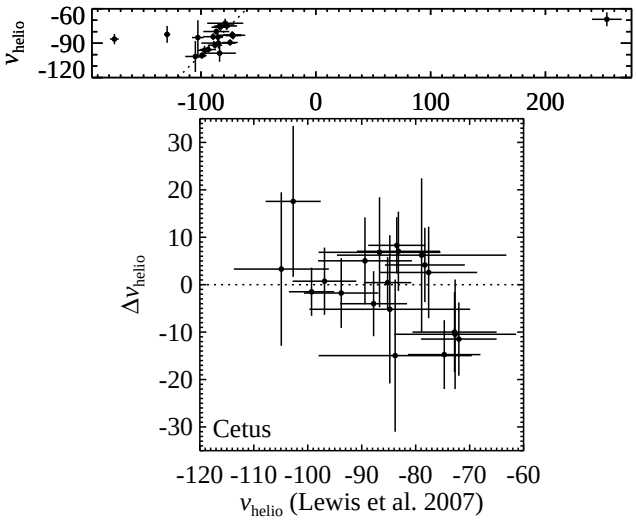

Figure 5. Comparison of radial velocities of the stars in common between our work and that of Lewis et al. (2007). The top panel shows all 23 stars in common. The bottom panel shows the 20 stars in the range $-120 < v_{\rm helio} < -60$ km s^{-1}. The dotted lines indicate equality.

3.1 Comparison to previous measurements

Lewis et al. (2007) measured radial velocities for 70 stars in the vicinity of Cetus. Fig. 5 presents the comparison of the radial velocity measurements of the 23 stars that overlap with our sample. The velocity differences, $\Delta v_{\rm helio}$, are distributed as expected based on the estimated uncertainties for 20 stars. The remaining three stars are highly discrepant between the two samples. We would not have considered these stars members of Cetus based on Lewis et al.'s velocities, but our velocities are within our membership cuts. We confirmed that the radial velocity template spectra line up with our observed spectra with our velocities but not with Lewis et al.'s velocities. The differences in velocities between the two studies is probably due to the longer exposure times and higher S/N of our spectra.

4 MEMBERSHIP

Not every star that we targeted is a member of its respective galaxy. We assigned binary (yes or no) membership to each star based on its position in the colour–magnitude diagram, the equivalent width (EW) of its Na I λ8190 doublet and its radial velocity. We used only member stars to compute average radial velocities and velocity dispersions of the dwarf galaxies.

4.1 Colour–magnitude diagram

The selection in the colour–magnitude diagram was accomplished in the slitmask design before the spectra were obtained. Only stars with reasonable colours and magnitudes for red giants were allowed. Fig. 2 of this paper, fig. 1 of Kirby et al. (2012) and figs. 2–6 of Kirby et al. (2013b) show that all of the stars deemed to be members are indeed on the red giant branch.

4.2 Na doublet

The Na I doublet at 8183 and 8195 Å is a good indicator of surface gravity (Spinrad & Taylor 1971; Cohen 1978; Schiavon et al. 1997; Gilbert et al. 2006). Dwarf stars,

which have high surface gravities, have strong Na doublets. Kirby et al. (2012) showed that the combined EW of the doublet exceeds 1 Å only in stars with surface gravities $\log g > 4.5$ as long as [Na/H] ≤ 0, which is a reasonable assumption for these metal-poor galaxies (Kirby et al. 2013b).

We computed EWs for each line in the doublet by fitting Gaussian or Lorentzian profiles. For weak doublets, Gaussians were better fits. For very strong doublets in dwarf stars, Lorentzian profiles better matched the damping wings of the absorption lines. In most stars, the doublet was not detectable above the noise. For those stars where it was possible to measure EWs, we also computed errors by Monte Carlo resampling of the spectra in the same manner used to compute velocity errors (see Sec. 3).

We ruled as non-members those stars where the combined EW of the two lines exceeded 1 Å, even after accounting for the error in the EW measurements. In other words, for a star to be counted as a non-member, its Na I EW needed to exceed 1 Å by at least 1σ. Stars ruled as non-members on the basis of Na I EW are indicated by 'Na' in the last column of Table 2.

4.3 Radial velocity

Some stars have radial velocities inconsistent with the radial velocity of the galaxy. We interpret these interlopers as foreground stars in the Milky Way. We set the exclusion limits at 2.58 times the velocity dispersion (determined in Sec. 5). This range includes 99 per cent of the member stars assuming a normal velocity distribution. It excludes non-members at the cost of also excluding 1 per cent of members.

However, we retained stars with velocity errors within 1σ of the allowed range of velocities. For example, we measured the mean velocity of IC 1613 to be $\langle v_{\rm helio} \rangle = -231.6$ km s^{-1} with a velocity dispersion of $\sigma_v = 10.8$ km s^{-1}. Therefore, the range of allowed velocities is $-259.5 < v_{\rm helio} < -203.8$ km s^{-1}. Star B07-56088 has a radial velocity of -198.0 ± 14.1 km s^{-1}. Although the velocity of this star is outside of the membership limits, we still counted it as a member because its 1σ error bar reaches the upper range of velocities that qualify for membership in IC 1613.

The membership list affects the measurements of $\langle v_{\rm helio} \rangle$ and σ_v, but the membership criteria depend on those measurements. Therefore, the membership determination was iterative. We started with guesses at $\langle v_{\rm helio} \rangle$ and σ_v, determined from fitting a Gaussian to a velocity histogram. Then, we determined membership for each star based on radial velocity, and we calculated $\langle v_{\rm helio} \rangle$ and σ_v following the procedure described in Sec. 5. We performed a new membership cut based on these new values, and we repeated the process until the membership list did not change from one iteration to the next.

Stars that were excluded on the basis of radial velocity are indicated by 'v' in the last column of Table 2. Stars ruled as non-members from either Na I EW or radial velocity are shown as hollow circles in Figs. 1 and 2.

5 VELOCITY DISPERSIONS

We measured $\langle v_{\rm helio} \rangle$ and σ_v with a Monte Carlo Markov chain (MCMC). Following the procedure for measuring velocity dispersions introduced by Walker et al. (2006a), we maximized the likelihood (L) that the values of $\langle v_{\rm helio} \rangle$ and σ_v accurately described the observed velocity distribution of member stars, accounting for uncertainties in the individual velocity measurements. The logarithm of the likelihood is

$$\begin{aligned} \log L &= \frac{N \log(2\pi)}{2} + \frac{1}{2} \sum_i^N \left(\log((\delta v_r)_i^2 + \sigma_v^2) \right) \\ &+ \frac{1}{2} \sum_i^N \left(\frac{((v_{\rm helio})_i - \langle v_{\rm helio} \rangle)^2}{(\delta v_r)_i^2 + \sigma_v^2} \right) \end{aligned} \quad (1)$$

where N is the number of member stars and $(v_{\rm helio})_i$ and $(\delta v_r)_i$ are the velocity and error for star i.

The MCMC had a length of 10^7 trials. We implemented the Metropolis–Hastings algorithm with normally distributed proposal densities. The standard deviation of both the $\langle v_{\rm helio} \rangle$ and σ_v proposal densities was 5 km s^{-1}. The values for each iteration (j) were perturbed from the previous iteration ($j-1$) according to these proposal densities. If the likelihood increased or if $\exp(L_j - L_{j-1})$ was greater than a random number selected from a uniform distribution between 0 and 1, then the new values of $\langle v_{\rm helio} \rangle$ and σ_v from iteration j were accepted. Otherwise, they were discarded and the next iteration began with the original values of $\langle v_{\rm helio} \rangle$ and σ_v from iteration $j-1$.

The final values of $\langle v_{\rm helio} \rangle$ and σ_v were set to be the mean values of the successful links in the MCMC. The asymmetric 1σ confidence intervals were determined from the values that enclosed 68.3 per cent of the successful MCMC links. Table 3 gives these values for each of the seven dwarf galaxies in our sample, along with the distances, V-band luminosities, and half-light radii. The table lists the original sources for every measurement, but we adopted McConnachie's (2012) conversions from various scale radii to half-light radii in cases where the original sources did not quote half-light radii. The table also gives these values from the literature for all of the other Local Group galaxies with $10^5 < L_V/{\rm L}_\odot < 2 \times 10^8$ whose velocity dispersions have been measured. The luminosity cut restricts the satellite galaxies to about the same stellar mass range as the isolated galaxies. For the galaxies in our sample, the table indicates the number of member stars (N). The table also gives the total dynamical mass enclosed within the deprojected, three-dimensional half-light radius ($M_{1/2}$) from the formula of Wolf et al. (2010). The 3-D half-light radius, $r_{1/2}$, is well approximated by $\frac{4}{3} r_h$, where r_h is the 2-D, projected half-light radius.

$$M_{1/2} = 4 G^{-1} \sigma_v^2 r_h = 3 G^{-1} \sigma_v^2 r_{1/2} \quad (2)$$

We also calculated the mass-to-light ratio within $r_{1/2}$ ($(M/L_V)_{1/2}$). The errors on $M_{1/2}$ and $(M/L_V)_{1/2}$ include errors on the distance, L_V, r_h and σ_v.

Fig. 6 shows the velocity distributions of the seven dwarf galaxies. Non-member stars not included in the measurements of the velocity dispersions are shaded. The maximum likelihood values of $\langle v_{\rm helio} \rangle$ are shown as vertical dotted lines.

Table 3. Structural and dynamical quantities for Local Group galaxies with $10^5 < L_V/\mathrm{L}_\odot < 2 \times 10^8$.

Galaxy	Distance (kpc)	L_V (10^6 $\mathrm{L}_\odot$)	r_h (pc)	N	$\langle v_\mathrm{helio} \rangle$ (km s^{-1})	σ_v (km s^{-1})	$M_{1/2}$ (10^6 $\mathrm{M}_\odot$)	$(M/L_V)_{1/2}$ ($\mathrm{M}_\odot$ $\mathrm{L}_\odot^{-1}$)
Isolated (this work)								
IC 1613	758 ± 4^{c}	$100\ ^{+20}_{-10}{}^{d}$	1040 ± 65^{e}	139	-231.6 ± 1.2	$10.8\ ^{+1.0}_{-0.9}$	110 ± 20	2.2 ± 0.5
NGC 6822	459 ± 8^{f}	98 ± 18^{g}	478 ± 28^{e}	292	-54.5 ± 1.7	23.2 ± 1.2	240 ± 30	4.9 ± 1.1
VV 124	1361 ± 25^{h}	$9.0\ ^{+1.8}_{-1.5}{}^{i}$	272 ± 27^{i}	67	-29.2 ± 1.6	$9.6\ ^{+1.3}_{-1.2}$	$23\ ^{+7}_{-6}$	$5.2\ ^{+1.8}_{-1.7}$
Pegasus	920 ± 29^{j}	$6.6\ ^{+1.4}_{-1.2}{}^{d}$	695 ± 37^{e}	103	-179.5 ± 1.5	$12.3\ ^{+1.2}_{-1.1}$	130 ± 10^{a}	39 ± 8^{a}
Leo A	787 ± 4^{k}	$6.0\ ^{+1.4}_{-1.2}{}^{d}$	354 ± 19^{e}	48	24.0 ± 1.5	$6.7\ ^{+1.4}_{-1.2}$	$15\ ^{+6}_{-5}$	$5.0\ ^{+2.3}_{-2.1}$
Cetus	779 ± 43^{l}	3.0 ± 0.6^{m}	612 ± 38^{m}	116	-83.9 ± 1.2	8.3 ± 1.0	$40\ ^{+10}_{-9}$	27 ± 9
Aquarius	1071 ± 39^{j}	1.2 ± 0.1^{n}	342 ± 15^{n}	27	-137.7 ± 2.1	$7.9\ ^{+1.9}_{-1.6}$	$20\ ^{+10}_{-8}$	$32\ ^{+16}_{-14}$
Isolated (literature)								
WLM	933 ± 34^{j}	43 ± 5^{d}	1569 ± 74^{o}		-130.0 ± 1.0	17.0 ± 1.0^{o}	$630 \pm 30^{a,b}$	$30 \pm 4^{a,b}$
Tucana	887 ± 49^{l}	0.59 ± 0.12^{p}	209 ± 34^{p}		194.0 ± 4.3	$15.8\ ^{+4.1}_{-3.1}{}^{q}$	71 ± 12^{a}	240 ± 60^{a}
Leo T	398 ± 36^{r}	0.14 ± 0.04^{r}	114 ± 12^{r}		38.1 ± 2.0	7.5 ± 1.6^{s}	6.0 ± 2.6	89 ± 46
Milky Way								
Sagittarius	26 ± 1^{t}	21 ± 6^{u}	1551 ± 118^{u}		140.0 ± 2.0	9.9 ± 0.7^{v}	140 ± 20	14 ± 5
Fornax	147 ± 9^{w}	20 ± 6^{x}	710 ± 70^{x}		55.1 ± 0.3	11.8 ± 0.2^{y}	91 ± 10	9.0 ± 2.7
Leo I	253 ± 15^{z}	5.6 ± 1.5^{x}	250 ± 26^{x}		282.8 ± 0.6	8.8 ± 0.5^{aa}	18 ± 3	$6.5\ ^{+2.1}_{-2.0}$
Sculptor	85 ± 4^{bb}	2.3 ± 1.1^{x}	282 ± 42^{x}		111.4 ± 0.3	9.2 ± 0.2^{y}	22 ± 4	20 ± 10
Leo II	233 ± 13^{cc}	0.75 ± 0.21^{x}	176 ± 42^{x}		78.0 ± 0.7	6.6 ± 0.7^{dd}	7.1 ± 2.3	19 ± 8
Sextans	85 ± 3^{ee}	0.44 ± 0.20^{x}	694 ± 43^{x}		224.2 ± 0.5	7.9 ± 0.4^{y}	$40\ ^{+4}_{-5}$	180 ± 90
Carina	106 ± 7^{w}	0.37 ± 0.17^{x}	254 ± 40^{x}		223.1 ± 0.4	6.7 ± 0.3^{y}	11 ± 2	57 ± 28
Ursa Minor	75 ± 3^{ff}	0.27 ± 0.13^{x}	180 ± 27^{x}		-246.9 ± 0.8	9.5 ± 1.2^{gg}	15 ± 4	110 ± 60
Draco	75 ± 5^{hh}	0.27 ± 0.05^{ii}	$220\ ^{+16}_{-15}{}^{ii}$		-291.0 ± 0.7	9.1 ± 1.2^{dd}	17 ± 5	130 ± 40
Can. Ven. I	217 ± 23^{jj}	$0.24\ ^{+0.05}_{-0.07}{}^{ii}$	564 ± 64^{ii}		30.9 ± 0.6	7.6 ± 0.4^{s}	30 ± 5	260 ± 80
M31								
NGC 185	$619\ ^{+19}_{-17}{}^{kk}$	$68\ ^{+9}_{-8}{}^{d}$	$459\ ^{+91}_{-90}{}^{d}$		-203.8 ± 1.1	24.0 ± 1.0^{ll}	290 ± 60^{a}	8.7 ± 2.0^{a}
NGC 147	711 ± 19^{kk}	$62\ ^{+8}_{-7}{}^{d}$	655 ± 104^{d}		-193.1 ± 0.8	16.0 ± 1.0^{ll}	240 ± 40^{a}	7.9 ± 1.6^{a}
And VII	762 ± 35^{j}	17 ± 5^{m}	731 ± 36^{m}		-307.2 ± 1.3	13.0 ± 1.0^{mm}	110 ± 20	13 ± 4
And II	630 ± 14^{kk}	8.6 ± 1.6^{m}	1027 ± 30^{m}		-192.4 ± 0.5	7.8 ± 1.1^{nn}	110 ± 0^{a}	27 ± 5^{a}
And I	727 ± 16^{kk}	4.5 ± 0.5^{m}	592 ± 25^{m}		-376.3 ± 2.2	10.2 ± 1.9^{mm}	57 ± 22	26 ± 10
And VI	783 ± 25^{j}	3.4 ± 0.7^{m}	410 ± 20^{m}		-339.8 ± 1.8	$12.4\ ^{+1.5}_{-1.3}{}^{oo}$	$59\ ^{+14}_{-13}$	$35\ ^{+11}_{-10}$
LGS 3	769 ± 24^{j}	1.1 ± 0.1^{pp}	469 ± 47^{pp}		-282.2 ± 3.5	$7.9\ ^{+5.3}_{-2.9}{}^{qq}$	$27\ ^{+37}_{-20}$	$49\ ^{+66}_{-37}$
And XXIII	$748\ ^{+31}_{-20}{}^{kk}$	0.97 ± 0.45^{rr}	$1001\ ^{+60}_{-51}{}^{rr}$		-237.7 ± 1.2	7.1 ± 1.0^{oo}	$47\ ^{+14}_{-13}$	96 ± 52
And III	$724\ ^{+16}_{-23}{}^{kk}$	0.93 ± 0.26^{m}	$337\ ^{+19}_{-20}{}^{m}$		-344.3 ± 1.7	9.3 ± 1.4^{mm}	27 ± 8	58 ± 24
And XXI	$827\ ^{+22}_{-26}{}^{kk}$	0.78 ± 0.43^{ss}	$842\ ^{+75}_{-77}{}^{ss}$		-361.4 ± 5.8	7.2 ± 5.5^{mm}	< 150	< 390
And XXV	$734\ ^{+23}_{-71}{}^{kk}$	0.53 ± 0.24^{rr}	$640\ ^{+47}_{-75}{}^{rr}$		-107.8 ± 1.0	$3.0\ ^{+1.2}_{-1.1}{}^{oo}$	$5.4\ ^{+4.3}_{-4.0}$	$20\ ^{+19}_{-18}$
And V	$741\ ^{+20}_{-23}{}^{kk}$	0.52 ± 0.10^{m}	$280\ ^{+19}_{-20}{}^{m}$		-397.3 ± 1.5	10.5 ± 1.1^{mm}	29 ± 6	110 ± 30
And XV	$625\ ^{+74}_{-34}{}^{kk}$	0.49 ± 0.18^{tt}	$220\ ^{+27}_{-15}{}^{tt}$		-323.0 ± 1.4	4.0 ± 1.4^{mm}	3.3 ± 2.3	13 ± 11
And XIX	$820\ ^{+30}_{-162}{}^{kk}$	0.45 ± 0.25^{uu}	$1479\ ^{+59}_{-293}{}^{uu}$		-111.6 ± 1.5	$4.7\ ^{+1.6}_{-1.4}{}^{oo}$	$30\ ^{+21}_{-19}$	$140\ ^{+120}_{-110}$
And XVI	$476\ ^{+41}_{-30}{}^{kk}$	0.41 ± 0.15^{tt}	$123\ ^{+12}_{-10}{}^{tt}$		-367.3 ± 2.8	3.8 ± 2.9^{mm}	< 5.9	< 30
And XXVII	$1253\ ^{+40}_{-594}{}^{kk}$	0.28 ± 0.13^{rr}	$656\ ^{+111}_{-329}{}^{rr}$		-539.6 ± 4.6	$14.8\ ^{+4.3}_{-3.1}{}^{oo}$	$130\ ^{+80}_{-90}$	$940\ ^{+720}_{-760}$
And XVII	$727\ ^{+36}_{-26}{}^{kk}$	0.24 ± 0.07^{vv}	$262\ ^{+21}_{-19}{}^{vv}$		-251.6 ± 1.9	$2.9\ ^{+2.2}_{-1.9}{}^{oo}$	< 7.3	< 62
And XIV	$794\ ^{+21}_{-204}{}^{kk}$	$0.24\ ^{+0.23}_{-0.09}{}^{ww}$	$392\ ^{+185}_{-210}{}^{ww}$		-480.6 ± 1.2	5.3 ± 1.0^{mm}	$10\ ^{+6}_{-7}$	$87\ ^{+71}_{-74}$
And XXVIII	$660\ ^{+152}_{-60}{}^{xx}$	$0.21\ ^{+0.20}_{-0.08}{}^{xx}$	$213\ ^{+63}_{-44}{}^{xx}$		-331.1 ± 1.8	4.9 ± 1.6^{yy}	$4.8\ ^{+3.4}_{-3.3}$	$44\ ^{+43}_{-42}$
And XXIX	731 ± 74^{zz}	0.18 ± 0.07^{zz}	361 ± 56^{zz}		-194.4 ± 1.5	5.7 ± 1.2^{yy}	11 ± 5	120 ± 70
And IX	$599\ ^{+85}_{-22}{}^{kk}$	$0.15\ ^{+0.01}_{-0.05}{}^{ab}$	$432\ ^{+64}_{-87}{}^{ab}$		-209.4 ± 2.5	10.9 ± 2.0^{mm}	$48\ ^{+19}_{-20}$	$640\ ^{+290}_{-310}$
And XXX	$682\ ^{+31}_{-81}{}^{kk}$	$0.13\ ^{+0.06}_{-0.03}{}^{oo}$	$267\ ^{+26}_{-48}{}^{oo}$		-139.8 ± 6.3	$11.8\ ^{+7.7}_{-4.7}{}^{oo}$	$35\ ^{+45}_{-28}$	$530\ ^{+710}_{-460}$

The 2-D, projected half-light radius (r_h) is related to the 3-D, de-projected half-light radius ($r_{1/2}$) by $r_{1/2} \simeq \frac{4}{3} r_h$. The last two columns give the mass and mass-to-light ratio within $r_{1/2}$. L_V, $M_{1/2}$ and $(M/L_V)_{1/2}$ are quoted with two significant digits. Where the error bars include zero, 2σ upper limits are given.

[a] $M_{1/2}$ and $(M/L_V)_{1/2}$ include a contribution from rotation (see Sec. 5.2).

[b] Leaman et al. (2012) calculated $M_{1/2} = (4.3 \pm 0.3) \times 10^8$ $\mathrm{M}_\odot$ based on a sophisticated dynamical model that is more appropriate for a rotating system than our modification to Wolf et al.'s (2010) formula for $M_{1/2}$ (Sec. 5.2). Leaman et al.'s value of $M_{1/2}$ implies $(M/L_V)_{1/2} = 20.1 \pm 2.8$ $\mathrm{M}_\odot$ $\mathrm{L}_\odot^{-1}$.

[c] Bernard et al. (2010) [d] de Vaucouleurs et al. (1991) [e] Hunter & Elmegreen (2006) [f] Gieren et al. (2006)

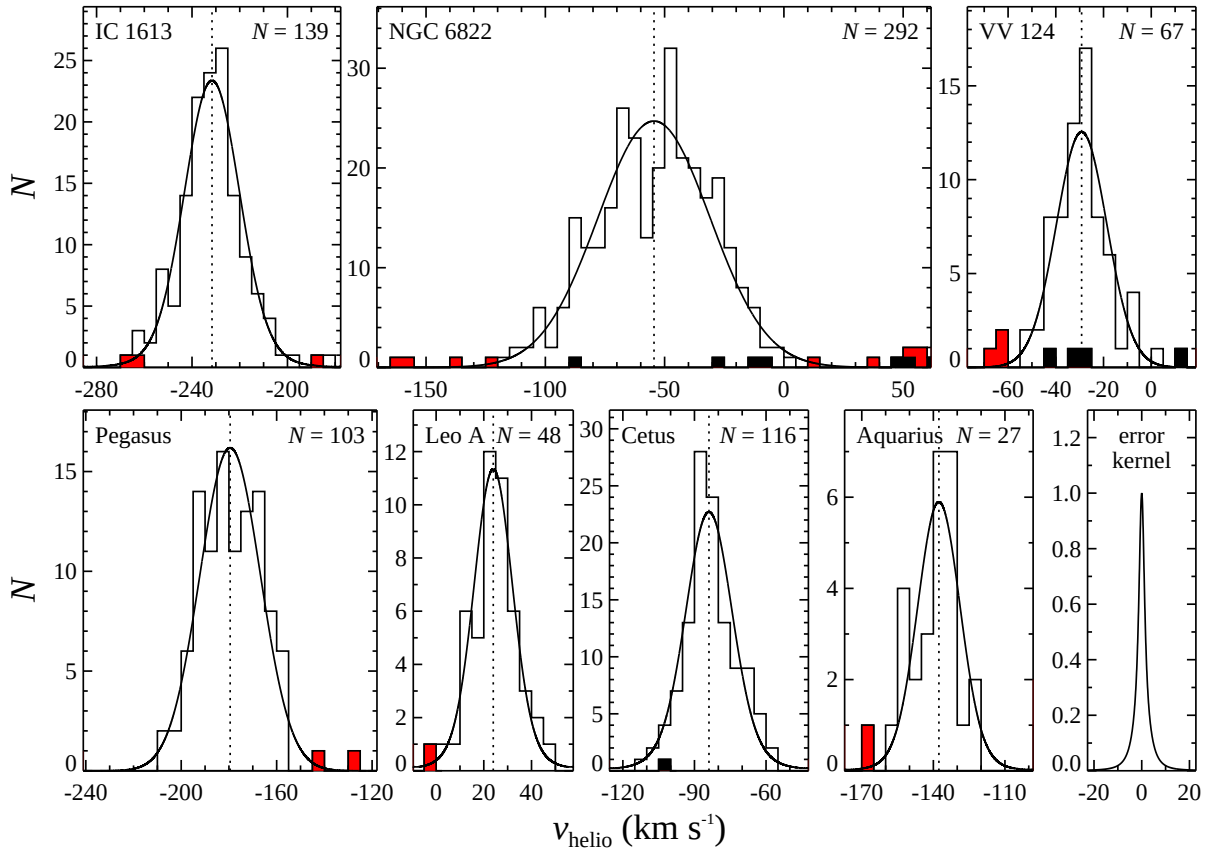

Figure 6. Heliocentric radial velocity distributions. Unshaded regions of the histograms contain spectroscopically confirmed members. Black and red shaded regions indicate spectroscopic non-members from Na I λ8190 EW and radial velocity, respectively. The vertical dotted lines indicate $\langle v_{\rm helio} \rangle$. The solid curve is a Gaussian with the measured σ_v, convolved with the error kernel, which is shown in the bottom right panel. The bins are 5 km s^{-1} wide. The number of member stars is indicated in the upper right of each panel. The rotation curve has been removed from Pegasus (see Sec. 5.2).

Table 3 – *continued*

[g]Dale et al. (2007)
[j]McConnachie et al. (2005)
[m]McConnachie & Irwin (2006)
[p]Saviane, Held, & Piotto (1996)
[s]Simon & Geha (2007)
[v]Frinchaboy et al. (2012)
[y]Walker, Mateo, & Olszewski (2009a)
[bb]Pietrzyński et al. (2008)
[ee]Lee et al. (2009)
[hh]Bonanos et al. (2004)
[kk]Conn et al. (2012)
[nn]Ho et al. (2012)
[qq]Cook et al. (1999)
[tt]Ibata et al. (2007)
[ww]Majewski et al. (2007)
[zz]Bell, Slater, & Martin (2011)
[h]Jacobs et al. (2011)
[k]Bernard et al. (2013)
[n]McConnachie et al. (2006)
[q]Fraternali et al. (2009)
[t]Monaco et al. (2004)
[w]Pietrzyński et al. (2009)
[z]Bellazzini et al. (2004)
[cc]Bellazzini, Gennari, & Ferraro (2005)
[ff]Carrera et al. (2002)
[ii]Martin, de Jong, & Rix (2008)
[ll]Geha et al. (2010)
[oo]Collins et al. (2013)
[rr]Richardson et al. (2011)
[uu]McConnachie et al. (2008)
[xx]Slater, Bell, & Martin (2011)
[ab]Collins et al. (2010)
[i]Bellazzini et al. (2011)
[l]Bernard et al. (2009)
[o]Leaman et al. (2012)
[r]de Jong et al. (2008)
[u]Majewski et al. (2003)
[x]Irwin & Hatzidimitriou (1995)
[aa]Mateo, Olszewski, & Walker (2008)
[dd]Walker et al. (2007)
[gg]Walker et al. (2009b)
[jj]Martin et al. (2008)
[mm]Tollerud et al. (2012)
[pp]Lee (1995)
[ss]Martin et al. (2009)
[vv]Brasseur et al. (2011)
[yy]Tollerud et al. (2013)

The solid curves are Gaussians with the maximum likelihood value of σ_v. The curves have been widened by the estimated uncertainties on the radial velocities. In detail, we constructed an error kernel by stacking N unit-area Gaussians, where N is the number of member stars. Each Gaussian in the stack had a width equal to the velocity error of one member star. The Gaussians representing the velocity distributions were convolved with the error kernel before plotting in Fig. 6. The bottom right panel of Fig. 6 shows the error kernel.

5.1 Effect of membership

The measurement of velocity dispersion depends on the membership criteria. A strict membership cut generally leads to a lower σ_v, whereas including stars at the fringes

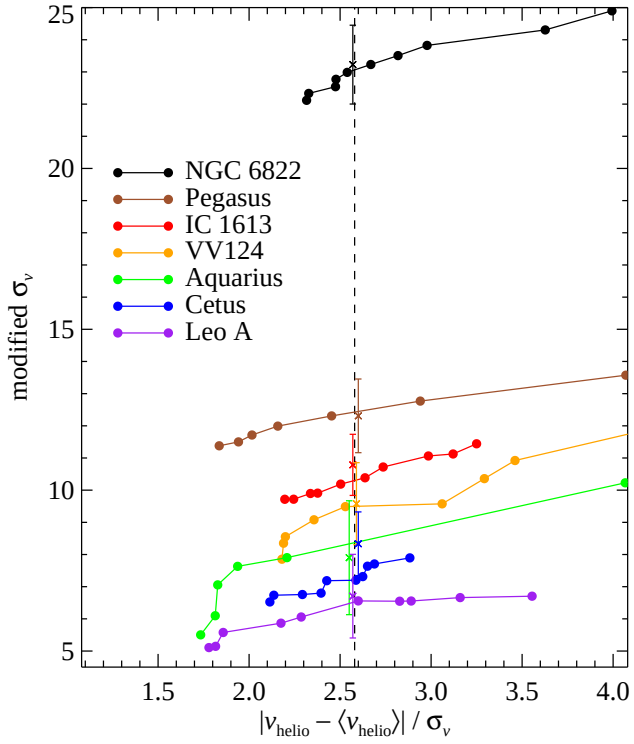

Figure 7. The effect on the velocity dispersion of excluding or including additional stars as members (see Sec. 5.1). The modified dispersions increase as additional stars are included. The x-axis shows the absolute difference between the added star's velocity and the galaxy's mean velocity in units of the originally measured velocity dispersion, shown as crosses (horizontally shifted for clarity). The dashed line shows our adopted membership cut, $2.58\sigma_v$. The crosses do not always intersect the curves at the dashed line because our final membership cut allows stars to the right of the line if their measurement uncertainties encompass $2.58\sigma_v$.

of the velocity distribution can inflate σ_v. Unfortunately, those same stars are also the stars with the most uncertain membership.

We explored the effect on σ_v of discarding and including stars in the membership lists. We started with a membership list with all stars within $2.58\sigma_v$ of $\langle v_{\rm helio}\rangle$. This membership list is not identical to that described in Sec. 4, which included stars beyond $2.58\sigma_v$ as long as their error bars encompassed $\langle v_{\rm helio}\rangle$. For simplicity, the membership cut for the purposes of this test is a strict cut regardless of the stars' velocity uncertainties. From this list, we removed the star with the velocity farthest from $\langle v_{\rm helio}\rangle$ and recomputed σ_v with 10^6 MCMC trials. We continued removing up to five stars. Then we added up to five stars to the strict membership list with velocities more than $2.58\sigma_v$ discrepant from $\langle v_{\rm helio}\rangle$.

Fig. 7 shows the result of this test. As expected, σ_v increases as stars farther removed from $\langle v_{\rm helio}\rangle$ are included. The effect of adding an additional star depends not only on its deviance from $\langle v_{\rm helio}\rangle$ but also its measurement uncertainty. For example, the extra stars in NGC 6822 have low velocity uncertainties. Therefore, adding them steadily increases σ_v. On the other hand, the extra stars in Leo A have large velocity uncertainties. Adding them has only a small effect on σ_v.

Because our final membership cut is not a strict cut at $2.58\sigma_v$, our final determinations of σ_v (crosses in Fig. 7) do not always intersect the curves at $2.58\sigma_v$. The effect of our soft membership cut is most apparent for Cetus, where our measurement of σ_v is about one standard deviation higher than if it were based on a strict membership cut. The soft membership cut is especially appropriate for galaxies, like Cetus, with velocity dispersions on the same order as the velocity uncertainties for individual stars. A strict membership cut for such galaxies would discard a larger fraction of stars than for galaxies with comparatively large σ_v. Even so, the difference in σ_v between a strict and soft membership cut is at most about 1 km s^{-1}.

Adding or removing stars between $2\sigma_v$ and $3.5\sigma_v$ affects σ_v by about ±1 km s^{-1}, which is on the order of the error on σ_v. We conclude that the choice of membership is important, but the exclusion of inclusion of a few stars does not alter σ_v by more than the errors quoted in Table 3.

5.2 Rotation

Fig. 8 shows the stellar velocities in Pegasus as a function of displacement along the major axis, assuming a sky position of $\alpha_0 = 23^{\rm h}28^{\rm m}36^{\rm s}$, $\delta_0 = +14^\circ44'35''$ and a position angle of 122° (Hunter & Elmegreen 2006). The stars are clearly rotating. We calculated the mean $v_{\rm helio}$ separately on the east and west sides of the minor axis. Half of the difference between the two velocities is 10.0 ± 0.3 km s^{-1}, where the error is the standard error on the mean. We take this value to be the projected rotation of the stars, $v \sin i$.

Young et al. (2003) measured the H I density and velocity distribution of Pegasus. They also found a velocity gradient very similar to Fig. 8. They suggested that bubbles and random motions – rather than rotation – cause the velocity gradient in the gas because the gas is clumpy, and the density of gas on the east side of the galaxy is larger than on the west side. However, we found that the velocity gradient is also present in red giants. If the gas gradient were caused by short-term hydrodynamical events, like winds from a supernova, then those events would not affect the kinematics of the red giants, which were presumably born before the recent supernova. Instead, the stars are moving in the same direction and at the same velocity as the gas (see fig. 6 of Young et al. 2003). Therefore, we suggest that the H I gas is in fact rotating.

We modified our method of calculating σ_v in Pegasus to account for the rotation. We subtracted $v \sin i$ from the velocities of the stars in the eastern half of Pegasus, and we added $v \sin i$ to the western stars. In other words, we removed the rotation. The velocity histogram for Pegasus in Fig. 6 reflects this modification, which reduces σ_v. We also modified the calculation of $M_{1/2}$ to account for rotation support in addition to pressure support. We replaced σ_v^2 in Eq. 2 with $\sigma_v^2 + \frac{1}{2}(v \sin i)^2$ (Weiner et al. 2006). The coefficient on $(v \sin i)^2$ depends on the mass profile, but its exact value matters less than uncertainty in inclination and the assumption of spherical symmetry implicit in Eq. 2.

The stellar velocity distribution of Pegasus, shown in Fig. 8, might be modelled as solid body rotation (velocity linearly increasing with radius) just as well as flat rotation. Pegasus is part of Local Irregulars That Trace Luminosity Extremes, The H I Nearby Galaxy Survey (LITTLE THINGS, Hunter et al. 2012), a detailed H I survey of dIrrs

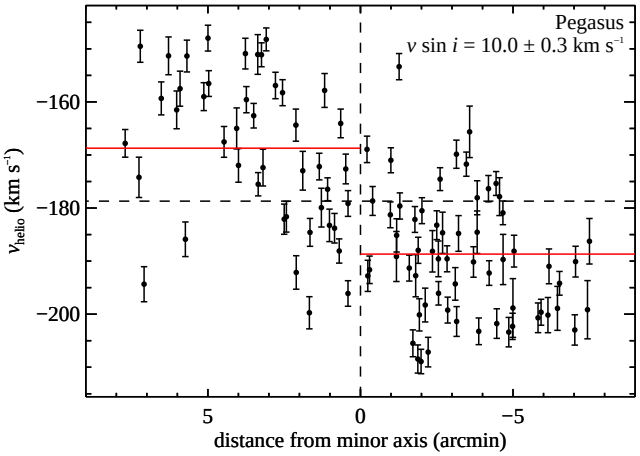

Figure 8. Rotation curve of Pegasus. The solid red lines show the mean velocity on the east (left/positive) and west (right/negative) sides of the major axis.

with velocity resolution of 2.6 km s^{-1}. A prospect for future work is to construct a dynamical model of Pegasus that combines our stellar velocities with the LITTLE THINGS gas map. That approach would allow not only a more accurate measurement of the dynamical mass of Pegasus but also a mass profile as function of radius.

We checked all of the other dwarf galaxies in our sample for stellar rotation. We found Pegasus to be the only galaxy in our sample with obviously rotating stars. (The gas may rotate or exhibit velocity structure independently from the stars, as shown by Lo, Sargent, & Young 1993. However, the gas and stars are independent tracers of mass. Gas rotation does not affect our conclusions based on stellar motions.) Demers et al. (2006) found that the carbon stars in the spheroid of NGC 6822 rotate perpendicular to the H I disc. The rotation curve seems to increase with radius. Their sample spanned an area of the galaxy about 2.5 times larger than our DEIMOS sample. Our more centrally concentrated sample has a hint of some velocity structure. It is possible that rotation on the order of ~ 10 km s^{-1} is present in our data, but the large velocity dispersion obscures the signal of rotation.

Two of the isolated galaxies that we did not observe are known to rotate. Leaman et al. (2012) measured a stellar rotation velocity of 17 ± 1 km s^{-1} in WLM. They constructed a dynamical model of the rotation of WLM in order to calculate $M_{1/2}$. Footnote *b* of Table 3 summarises their results. Their model is more appropriate than our simple modification to Wolf et al.'s (2010) formula to account for rotation. Fraternali et al. (2009) also measured rotation in Tucana. Tucana is faint (6×10^5 L$_\odot$), which makes building a spectroscopic sample challenging. As a result, the measurement of the rotation velocity is highly uncertain. Assuming a flat rotation curve, the rotation velocity is about 15 km s^{-1}. We assume an uncertainty of 5 km s^{-1}.

Four satellites of M31 are also known to rotate. NGC 205 (Geha et al. 2006) is too luminous for our consideration. NGC 147 and NGC 185 are dwarf elliptical galaxies with rotation velocities of 17 ± 2 and 15 ± 5 km s^{-1}, respectively (Geha et al. 2010). Finally, the dSph And II exhibits prolate rotation with a velocity of 10.9 ± 2.4 km s^{-1} (Ho et al. 2012). As with Pegasus, we incorporated the rotation velocities of WLM, Tucana, NGC 147, NGC 185, and And II into the derivation of $M_{1/2}$.

5.3 Comparison to previous measurements

Three of the galaxies in our sample have previous stellar velocity dispersion measurements in the literature. Tolstoy et al. (2001) measured $\sigma_v = 24.5$ km s^{-1} from 23 red giants in NGC 6822. They did not quote an uncertainty because they used the velocity dispersion only to determine membership. Regardless, their measurement is close to our value ($\sigma_v = 23.2 \pm 1.2$ km s^{-1}).

Lewis et al. (2007) measured $\sigma_v = 17 \pm 2$ km s^{-1} from red giants in Cetus. This measurement is approximately 4σ above our measurement of $\sigma_v = 8.3 \pm 1.0$ km s^{-1}. Part of the discrepancy is due to the classification of member stars. When we applied the same membership criteria (Sec. 4) and the same technique to measure σ_v (Sec. 5) to Lewis et al.'s catalogue of velocities, we obtained $\sigma_v = 12.0^{+2.0}_{-1.9}$ km s^{-1}, which lessens the difference between the samples to 1.7σ. The remaining difference may be due to the higher S/N of our sample and to differences in the details of measuring the velocities of individual stars. See Sec. 3.1 and Fig. 5 for a comparison of our measurements of individual stellar velocities to those of Lewis et al. (2007).

Brown et al. (2007) measured $\sigma_v = 9.3 \pm 1.3$ km s^{-1} from ten B supergiants and two H II regions in Leo A. They calculated this dispersion by subtracting the average measurement uncertainty in quadrature from the root mean square of the velocities. Their measurement is about 1σ above our measurement of $\sigma_v = 6.7^{+1.4}_{-1.2}$ km s^{-1}. We applied an MCMC with maximum likelihood (Eq. 1) to Brown et al.'s data, and we determined $\sigma_v = 10.8^{+3.7}_{-2.8}$ km s^{-1}, which is still a difference of 1.3σ from our measurement of σ_v from red giants. Although the discrepancy is not highly significant, it may be indicating an interesting difference between the dynamics of the young (B supergiants and H II regions) and old or intermediate-aged (red giants) stellar populations in Leo A. The apparent decrease of velocity dispersion with age is in contrast to the observed increase of velocity dispersion with age in WLM (Leaman et al. 2012).

6 DISCUSSION

A comparison of the kinematic and structural properties of isolated dwarf galaxies to those of the dwarf satellites of the Milky Way and M31 has the potential to shed light on a number of issues related to galaxy formation. Perhaps the leading model for the formation of dSphs is that these galaxies are the descendants of dIrrs that have been tidally harassed and stripped of their gas as a result of falling into a more massive halo (e.g., Lin & Faber 1983; Mayer et al. 2001; Kormendy & Bender 2012). Our results, as well as comparative studies of the metallicities of the two populations (Kirby et al. 2013b), place important constraints on this and related models of dwarf galaxy transformations. Similarly, they inform models that invoke strong tidal stripping and mass loss to explain the TBTF problem.

Fig. 9 shows σ_v versus the two-dimensional, projected

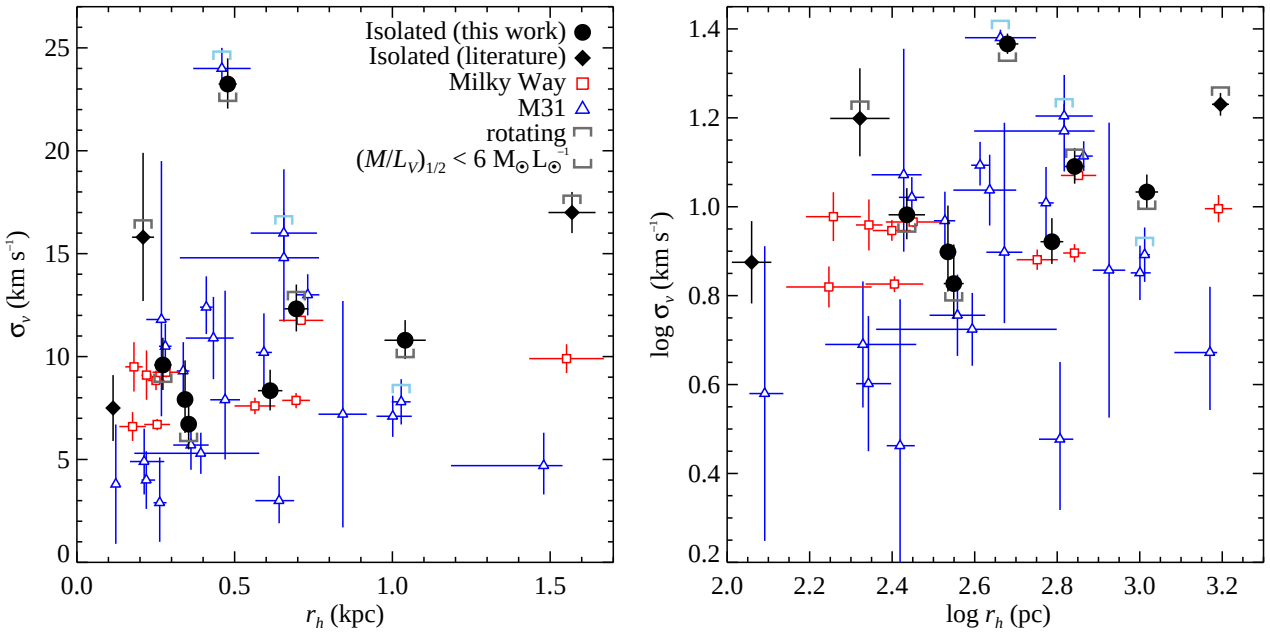

Figure 9. Velocity dispersion versus projected half-light radius for dwarf galaxies in the field (black circles), satellites of the Milky Way (red squares) and satellites of M31 (blue triangles). Only galaxies with $10^5 < L_V/\mathrm{L}_\odot < 2\times10^8$ are shown. Both panels show the same data on linear (left) and logarithmic (right) axes. The central masses of galaxies indicated with marks under the points have a significant component from baryons ($(M/L_V)_{1/2} < 6\ \mathrm{M}_\odot\ \mathrm{L}_\odot^{-1}$). The velocity dispersions for these galaxies from dark matter alone would be lower. Rotating galaxies are indicated by marks over the points. For these galaxies, the rotation-corrected velocities for mass estimation (see Sec. 5.2) are 15–40 per cent larger than σ_v.

r_h for both the isolated galaxies and satellites with $10^5 < L_V/\mathrm{L}_\odot < 2\times10^8$. This luminosity cut is intended to restrict the samples to about the same range of stellar mass. These data are the same as those presented in Table 3. The y-axis in Fig. 9 is intended to be a rough proxy for the mass of the galaxy. Marks over points indicate galaxies with significant rotation (Pegasus, WLM, Tucana, and And II). A complete estimate of the mass would include the rotation. The values of $M_{1/2}$ in Table 3 include rotation by replacing σ_v^2 in Eq. 2 with $\sigma_v^2 + \frac{1}{2}(v\sin i)^2$ (Weiner et al. 2006, see Sec. 5.2). The modified velocity dispersion is 15–40 per cent larger than σ_v for the rotating galaxies.

We use stellar velocities to trace the mass distribution. For many galaxies, the mass distribution is dominated by dark matter. However, the stars of some galaxies are centrally concentrated enough that the stellar velocities are about as sensitive to stellar mass as dark matter mass. Furthermore, most of the isolated dIrrs have gas masses of the same order as the stellar masses. Mass models of the dark matter subhaloes must take these baryons into account. Fig. 9 identifies galaxies where baryons are especially important ($(M/L_V)_{1/2} < 6\ \mathrm{M}_\odot\ \mathrm{L}_\odot^{-1}$).

The two samples are not distinct in the σ_v–r_h plane. A two-dimensional Kolmogorov–Smirnov (K–S) test yields a 51 per cent probability that the isolated galaxies are drawn from the same parent population as Milky Way and M31 satellites. This statistic increases to 65 per cent if $\sqrt{\sigma_v^2 + \frac{1}{2}(v\sin i)^2}$ is used for the four rotating galaxies instead of σ_v. However, we caution that empirical distribution function tests, like the K–S and Anderson–Darling tests, are technically invalid in more than one dimension because there is not a unique ordering of data points (Feigelson & Babu 2012).

Even in the absence of a rigorous statistical test, Fig. 9 shows that there is no obvious distinction between the isolated dwarf galaxies and the satellites. WLM is the farthest outlying galaxy, with both a high σ_v and a high r_h compared to the bulk of the other galaxies. At least part of the difference is due to the fact that WLM is a dIrr whereas all of the satellite galaxies in Table 3 and Fig. 9 are dSphs. Besides WLM, other dIrrs have some distinctions from the dSphs. Although there may be hints of rotation in Fornax and Sculptor (Walker et al. 2006a; Battaglia et al. 2008), only some of the most luminous M31 dSphs – NGC 147, NGC 185, NGC 205, and And II (Geha et al. 2006, 2010; Ho et al. 2012) – have clear stellar rotation curves. On the other hand, dIrrs as faint as Pegasus ($L_V = 7\times10^6\ \mathrm{L}_\odot$) and Tucana ($L_V = 6\times10^5\ \mathrm{L}_\odot$) are rotating. Whereas dSphs mostly have flat velocity dispersions as a function of radius (e.g., Walker et al. 2006a,b; Battaglia et al. 2008), the velocity dispersion of WLM decreases with radius (Leaman et al. 2012). The ellipticities of the dIrrs are larger on average than the dSphs, perhaps due to the presence of rotating discs in some dIrrs. The most obvious difference is the presence of gas in the dIrrs but not the dSphs (Grcevich & Putman 2009). Together, all of these pieces of evidence will provide strong constraints on models of the formation and evolution of dwarf galaxies, especially the possible transformation of dIrrs to dSphs.

Although proximity to a large host definitely influences the kinematics (support by rotation versus dispersion), structure (ellipticity) and gas content of dwarf galaxies, it is not clear that environment can explain the TBTF problem.

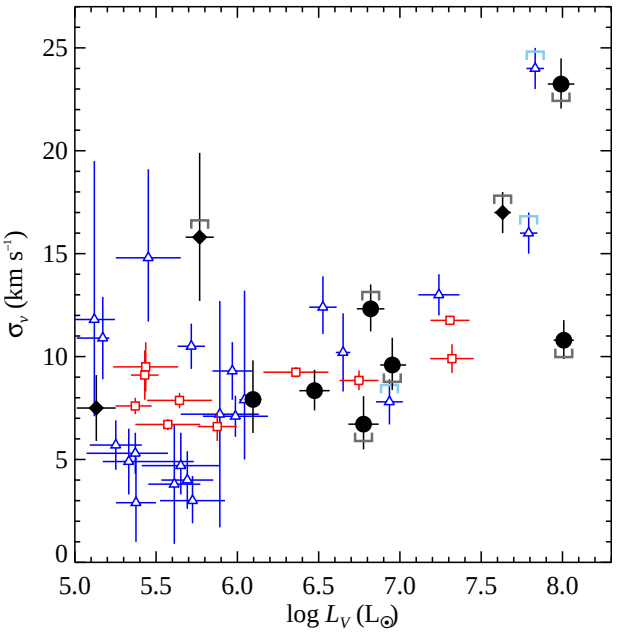

Figure 10. Velocity dispersion versus luminosity for Local Group dwarf galaxies. The symbols are the same as in Fig. 9.

TBTF can be viewed in terms of the maximum circular velocity of a subhalo ($v_{\rm max}$) and its radius when it achieved that circular velocity ($r_{\rm max}$). Both $v_{\rm max}$ and $r_{\rm max}$ are derived from the directly observable quantities σ_v and r_h. Because the isolated and satellite galaxies are not obviously distinct in the σ_v–r_h plane, environment is not an obvious cause of TBTF.

Another way to frame TBTF is that dark matter simulations predict more dense satellites than are observed. However, the field of the Local Group has no galaxy denser than the densest satellite of the MW or M31. Therefore, the isolated galaxies, which are minimally affected by the gravitational and ram pressure influences of the large spiral galaxies, also exhibit the same range of structural properties that give rise to the TBTF problem for satellite galaxies.

Of course, the Milky Way and M31 do tidally disturb some of their dSph satellites, like Sagittarius (Ibata, Gilmore, & Irwin 1994) and Hercules (Deason et al. 2012). Brooks & Zolotov (2012) predicted that these tidal forces would cause satellite galaxies to have a lower circular velocity than field dwarf galaxies in the same luminosity range. Fig. 10 shows velocity dispersions (not circular velocities) versus luminosities for both field and satellite dwarf galaxies. Circular velocities and velocity dispersions are not proportional when the stars are rotating, but most of the galaxies in our sample do not have stellar rotation. The galaxies do not separate any more in this space than in the space of velocity dispersion versus half-light radius. The 2-D K–S test between the field and satellite galaxies with $L_V/{\rm L}_\odot > 10^6$ returns a probability of 95 per cent that the galaxies are drawn from the same population. Accounting for rotational support reduces the probability only to 89 per cent. Therefore, our observations impose limitations on both (1) proposed mechanisms for the transformation of dIrrs into dSphs and (2) environmental solutions to TBTF whether the problem is considered in terms of half-light radius or luminosity.

We have considered only one dynamical tracer population: red giants. All of the galaxies in our sample except Cetus also have gas. We have also made only the most basic estimate of dynamical mass ($M_{1/2}$). A worthwhile prospect for future work is to construct detailed models of the mass profiles of the galaxies we observed. For example, Adams et al. (2012) constructed such a model for NGC 2976. Our individual stellar velocities are available in Table 2 for interested modellers. Gas maps from LITTLE THINGS (Hunter et al. 2012) add value to the stellar velocities. Taken together, the stellar and gas kinematics can be used to make some of the most detailed mass profiles of galaxies yet. These profiles would be relevant to understanding the role of environment in the formation and evolution of dwarf galaxies, solving the TBTF problem and determining whether dwarf galaxies have cusped or cored dark matter profiles.

ACKNOWLEDGEMENTS

We are grateful to the many people who have worked to make the Keck Telescopes and their instruments a reality and to operate and maintain the Keck Observatory. The authors wish to extend special thanks to those of Hawaiian ancestry on whose sacred mountain we are privileged to be guests. Without their generous hospitality, none of the observations presented herein would have been possible.

We thank Josh Simon and Marla Geha for providing their DEIMOS radial velocity template spectra. We also thank Alan McConnachie and Mike Irwin for sharing their photometric and astrometric catalogue for Cetus. ENK acknowledges support from the Southern California Center for Galaxy Evolution, a multicampus research program funded by the University of California Office of Research, and partial support from NSF grant AST-1009973. JGC thanks NSF grant AST-0908139 for partial support.

REFERENCES

Adams J. J., Gebhardt K., Blanc G. A., Fabricius M. H., Hill G. J., Murphy J. D., van den Bosch R. C. E., van de Ven G., 2012, ApJ, 745, 92
Amorisco N. C., Zavala J., de Boer T. J. L., 2013, ApJL, submitted (arXiv:1309.5958)
Appenzeller I., et al., 1998, Messenger, 94, 1
Arraki K. S., Klypin A., More S., Trujillo-Gomez S., 2013, MNRAS, 2956
Battaglia G., Helmi A., Tolstoy E., Irwin M., Hill V., Jablonka P., 2008, ApJ, 681, L13
Bell E. F., Slater C. T., Martin N. F., 2011, ApJ, 742, L15
Bellazzini M., Gennari N., Ferraro F. R., Sollima A., 2004, MNRAS, 354, 708
Bellazzini M., Gennari N., Ferraro F. R., 2005, MNRAS, 360, 185
Bellazzini M., et al., 2011, A&A, 527, A58
Bernard E. J., et al., 2009, ApJ, 699, 1742
Bernard E. J., et al., 2010, ApJ, 712, 1259
Bernard E. J., et al., 2013, MNRAS, 432, 3047
Binggeli B., Tarenghi M., Sandage A., 1990, A&A, 228, 42

Bonanos A. Z., Stanek K. Z., Szentgyorgyi A. H., Sasselov D. D., Bakos G. Á., 2004, AJ, 127, 861
Boylan-Kolchin M., Bullock J. S., Kaplinghat M., 2011, MNRAS, 415, L40
Boylan-Kolchin M., Bullock J. S., Kaplinghat M., 2012, MNRAS, 422, 1203
Brasseur C. M., Martin N. F., Rix H.-W., Irwin M., Ferguson A. M. N., McConnachie A. W., de Jong J., 2011, ApJ, 729, 23
Brooks A. M., Kuhlen M., Zolotov A., Hooper D., 2013, ApJ, 765, 22
Brooks A. M., Zolotov A., 2012, ApJ, submitted (arXiv:1207.2468)
Brown W. R., Geller M. J., Kenyon S. J., Kurtz M. J., 2007, ApJ, 666, 231
Carrera R., Aparicio A., Martínez-Delgado D., Alonso-García J., 2002, AJ, 123, 3199
Cohen J. G., 1978, ApJ, 221, 788
Collins M. L. M., et al., 2010, MNRAS, 407, 2411
Collins M. L. M., et al., 2013, ApJ, 768, 172
Conn A. R., et al., 2012, ApJ, 758, 11
Cook K. H., Mateo M., Olszewski E. W., Vogt S. S., Stubbs C., Diercks A., 1999, PASP, 111, 306
Cooper M. C., Newman J. A., Davis M., Finkbeiner D. P., Gerke B. F., 2012, Astrophysics Source Code Library, record ascl:1203.003, 3003
Dalcanton J. J., et al., 2012, ApJS, 200, 18
Dale D. A., et al., 2007, ApJ, 655, 863
de Jong J. T. A., et al., 2008, ApJ, 680, 1112
de Vaucouleurs G., de Vaucouleurs A., Corwin H. G., Jr., Buta R. J., Paturel G., Fouqué P., 1991, Third Reference Catalogue of Bright Galaxies, Vol. 1–3. Springer, Berlin
Deason A. J., Belokurov V., Evans N. W., Watkins L. L., Fellhauer M., 2012, MNRAS, 425, L101
Demers S., Battinelli P., Kunkel W. E., 2006, ApJ, 636, L85
Faber S. M., et al., 2003, Proc. SPIE, 4841, 1657
Feigelson E. D., Babu J. G., 2012, Modern Statistical Methods for Astronomy. Cambridge Univ. Press, Cambridge
Fraternali F., Tolstoy E., Irwin M. J., Cole A. A., 2009, A&A, 499, 121
Frinchaboy P. M., Majewski S. R., Muñoz R. R., Law D. R., Łokas E. L., Kunkel W. E., Patterson R. J., Johnston K. V., 2012, ApJ, 756, 74
Garrison-Kimmel S., Rocha M., Boylan-Kolchin M., Bullock J. S., Lally J., 2013, MNRAS, 433, 3539
Geha M., Guhathakurta P., Rich R. M., Cooper M. C., 2006, AJ, 131, 332
Geha M., van der Marel R. P., Guhathakurta P., Gilbert K. M., Kalirai J., Kirby E. N., 2010, ApJ, 711, 361
Gieren W., Pietrzyński G., Nalewajko K., Soszyński I., Bresolin F., Kudritzki R.-P., Minniti D., Romanowsky A., 2006, ApJ, 647, 1056
Gilbert K. M., et al., 2006, ApJ, 652, 1188
Girardi L., Bertelli G., Bressan A., Chiosi C., Groenewegen M. A. T., Marigo P., Salasnich B., Weiss A., 2002, A&A, 391, 195
Grcevich J., Putman M. E., 2009, ApJ, 696, 385
Grebel E. K., Gallagher J. S., III, Harbeck D., 2003, AJ, 125, 1926
Guhathakurta P., Ostheimer J. C., Gilbert K. M., Rich R. M., Majewski S. R., Kalirai J. S., Reitzel D. B., Patterson R. J., 2005, preprint (arXiv:astro-ph/0502366)
Guhathakurta P., et al., 2006, AJ, 131, 2497
Helmi A., Sales L. V., Starkenburg E., Starkenburg T. K., Vera-Ciro C. A., De Lucia G., Li Y.-S., 2012, ApJ, 758, L5
Hook I. M., Jørgensen I., Allington-Smith J. R., Davies R. L., Metcalfe N., Murowinski R. G., Crampton D., 2004, PASP, 116, 425
Hunter D. A., Elmegreen B. G., 2006, ApJS, 162, 49
Hunter D. A., et al., 2012, AJ, 144, 134
Ho N., et al., 2012, ApJ, 758, 124
Ibata R. A., Gilmore G., Irwin M. J., 1994, Nature, 370, 194
Ibata R., Martin N. F., Irwin M., Chapman S., Ferguson A. M. N., Lewis G. F., McConnachie A. W., 2007, ApJ, 671, 1591
Irwin M., Hatzidimitriou D., 1995, MNRAS, 277, 1354
Irwin M. J., et al., 2007, ApJ, 656, L13
Jacobs B. A., Tully R. B., Rizzi L., Karachentsev I. D., Chiboucas K., Held E. V., 2011, EAS, 48, 67
Kirby E. N., Guhathakurta P., Sneden C., 2008, ApJ, 682, 1217
Kirby E. N., Guhathakurta P., Bolte M., Sneden C., Geha M. C., 2009, ApJ, 705, 328
Kirby E. N., Cohen J. G., Bellazzini M., 2012, ApJ, 751, 46
Kirby E. N., Boylan-Kolchin M., Cohen J. G., Geha M., Bullock J. S., Kaplinghat M., 2013a, ApJ, 770, 16
Kirby E. N., Cohen J. G., Guhathakurta P., Cheng L., Bullock J. S., Gallazzi A., 2013b, ApJ, 779, 102
Knapp G. R., Kerr F. J., Bowers P. F., 1978, AJ, 83, 360
Kormendy J., Bender R., 2012, ApJS, 198, 2
Leaman R., Cole A. A., Venn K. A., Tolstoy E., Irwin M. J., Szeifert T., Skillman E. D., McConnachie A. W., 2009, ApJ, 699, 1
Leaman R., et al., 2012, ApJ, 750, 33
Lee M. G., 1995, AJ, 110, 1129
Lee M. G., Yuk I.-S., Park H. S., Harris J., Zaritsky D., 2009, ApJ, 703, 692
Letarte B., et al., 2010, A&A, 523, A17
Lewis G. F., Ibata R. A., Chapman S. C., McConnachie A., Irwin M. J., Tolstoy E., Tanvir N. R., 2007, MNRAS, 375, 1364
Lin D. N. C., Faber S. M., 1983, ApJ, 266, L21
Lisker T., Grebel E. K., Binggeli B., Glatt K., 2007, ApJ, 660, 1186
Lo K. Y., Sargent W. L. W., Young K., 1993, AJ, 106, 507
Majewski S. R., Skrutskie M. F., Weinberg M. D., Ostheimer J. C., 2003, ApJ, 599, 1082
Majewski S. R., et al., 2007, ApJ, 670, L9
Martin N. F., et al., 2008, ApJ, 672, L13
Martin N. F., de Jong J. T. A., Rix H.-W., 2008, ApJ, 684, 1075
Martin N. F., et al., 2009, ApJ, 705, 758
Mateo M., Olszewski E. W., Walker M. G., 2008, ApJ, 675, 201
Mayer L., Governato F., Colpi M., Moore B., Quinn T., Wadsley J., Stadel J., Lake G., 2001, ApJ, 547, L123
McConnachie A. W., 2012, AJ, 144, 4
McConnachie A. W., Arimoto N., Irwin M., Tolstoy E., 2006, MNRAS, 373, 715
McConnachie A. W., Irwin M. J., 2006, MNRAS, 365, 1263

McConnachie A. W., Irwin M. J., Ferguson A. M. N., Ibata R. A., Lewis G. F., Tanvir N., 2005, MNRAS, 356, 979
McConnachie A. W., et al., 2008, ApJ, 688, 1009
McConnachie A. W., et al., 2009, Nature, 461, 66
Monaco L., Bellazzini M., Ferraro F. R., Pancino E., 2004, MNRAS, 353, 874
Newman J. A., et al., 2013, ApJS, 208, 5
Pasquini L., et al., 2002, Messenger, 110, 1
Peñarrubia J., Navarro J. F., McConnachie A. W., 2008, ApJ, 673, 226
Peñarrubia J., Pontzen A., Walker M. G., Koposov S. E., 2012, ApJ, 759, L42
Pietrzyński G., et al., 2008, AJ, 135, 1993
Pietrzyński G., Górski M., Gieren W., Ivanov V. D., Bresolin F., Kudritzki R.-P., 2009, AJ, 138, 459
Richardson J. C., et al., 2011, ApJ, 732, 76
Sales L. V., Navarro J. F., Abadi M. G., Steinmetz M., 2007, MNRAS, 379, 1475
Saviane I., Held E. V., Piotto G., 1996, A&A, 315, 40
Schiavon R. P., Barbuy B., Rossi S. C. F., Milone A., 1997, ApJ, 479, 902
Schlegel D. J., Finkbeiner D. P., Davis M., 1998, ApJ, 500, 525
Simon J. D., Geha M., 2007, ApJ, 670, 313
Slater C. T., Bell E. F., Martin N. F., 2011, ApJ, 742, L14
Spinrad H., Taylor B. J., 1971, ApJS, 22, 445
Teyssier M., Johnston K. V., Kuhlen M., 2012, MNRAS, 426, 1808
Tollerud E. J., et al., 2012, ApJ, 752, 45
Tollerud E. J., Geha M. C., Vargas L. C., Bullock J. S., 2013, ApJ, 768, 50
Tolstoy E., Irwin M. J., Cole A. A., Pasquini L., Gilmozzi R., Gallagher J. S., 2001, MNRAS, 327, 918
Walker M. G., Mateo M., Olszewski E. W., Bernstein R., Wang X., Woodroofe M., 2006a, AJ, 131, 2114
Walker M. G., Mateo M., Olszewski E. W., Pal J. K., Sen B., Woodroofe M., 2006b, ApJ, 642, L41
Walker M. G., Mateo M., Olszewski E. W., Gnedin O. Y., Wang X., Sen B., Woodroofe M., 2007, ApJ, 667, L53
Walker M. G., Mateo M., Olszewski E. W., 2009a, AJ, 137, 3100
Walker M. G., Mateo M., Olszewski E. W., Peñarrubia J., Wyn Evans N., Gilmore G., 2009b, ApJ, 704, 1274
Weiner B. J., et al., 2006, ApJ, 653, 1027
Weisz D. R., et al., 2011, ApJ, 739, 5
Wolf J., Martinez G. D., Bullock J. S., Kaplinghat M., Geha M., Muñoz R. R., Simon J. D., Avedo F. F., 2010, MNRAS, 406, 1220
Young L. M., van Zee L., Lo K. Y., Dohm-Palmer R. C., Beierle M. E., 2003, ApJ, 592, 111
Zolotov A., et al., 2012, ApJ, 761, 71